Article

Not peer-reviewed version

Density of States in the 3D System With Semimetallic Nodal-Loop and Insulating Gapped Phase

Zoran Rukelj , Ivan Kupčić , Danko Radić *

Posted Date: 31 October 2023

doi: 10.20944/preprints202310.2091.v1

Keywords: single-particle density of states; effective two-band Hamiltonian; 3D nodal-loop semimetals

doi:10.20944/preprints202310.2091.v1

Article

Density of States in the 3D System With Semimetallic Nodal-Loop and Insulating Gapped Phase

Zoran Rukelj, **Ivan Kupčić** and **Danko Radić** *

University of Zagreb, Faculty of Science, Department of Physics, Bijenička 32, 10000 Zagreb, Croatia
* Correspondence: dradic@phy.hr

Abstract: We investigate a single-particle density of states in the three-dimensional system described by effective two-band Hamiltonian which describes a ground state in two distant electronic phases: the semimetalic nodal-loop phase and the insulating gapped phase. Analysis of valence bands and Fermi surfaces in both phases indicates that the density of states crucially depends on the parameter in the Hamiltonian of the system that controls a topological alternation of the Fermi surface. The signature of that alternation is expected to play an important role in all quantities closely related to the density of electronic states, such as charge transport and optical conductivity of the system for example.

Keywords: single-particle density of states; effective two-band Hamiltonian; 3D nodal-loop semimetals

1. Introduction

Number of physical properties of solids, expectantly those related to charge transport, are often described by so-called effective electron Hamiltonian describing the domain spanned over a small portion of the Brillouin zone in a restricted energy interval around the Fermi energy. Based on the underlying symmetry of the crystal lattice, at the specific points of the Brillouin zone, a minimal multi-band Hamiltonian can be constructed, which is sufficient to describe some single-particle and collective models of the system [1]. One of such examples is the Bernevig-Hughes-Zhang Hamiltonian [2], appearing to be sufficient to describe electron properties of number of systems mapped to it. In the case when two bands are located near the Fermi level, and other bands are sufficiently far in energy, the minimal Hamiltonian can be further reduced to the two-band effective Hamiltonian represented by a 2×2 matrix. Electron bands of the two-band effective Hamiltonian have an electron-hole symmetry and, in multiple cases, they are simple enough to permit an analytical result for number of band-related calculations and obtained transport functions. Examples of systems whose electron bands are described by the two-band model are numerous, and can be easily found in all three dimensions. We mention just some notable examples like the Su–Schrieffer–Heeger model (SSH) [3] and Peierls model [4] in 1D, massless and massive 2D Dirac system [5–7], Weyl systems or multiple Weyl point systems [8–12], massless 3D Dirac [13], Mexican-hat systems [14–16], nodal-line systems [17], electron gas in a weak periodic potential [18], and so on.

In all mentioned systems, the single-particle and optical properties have been analytically derived, thus providing an insight into the underlying mechanisms and physical scales. In reality, however, many of specific properties that make the mentioned systems interesting are observed on small intrinsic energy scales no bigger then few meV around the Fermi energy. This makes it also challenging to experimentally distinguish different possible ground states from each other. For that sake, the single particle density of states (DOS) calculations are important, providing a direct information about electron bands. Those can be directly measured by, for example, measurement of DOS at the Fermi energy via Pauli paramagnetic susceptibility, or indirectly, as a part of the joint density of states approach to the inter-band conductivity [19]. Generally, the number of analytically solvable electron models is rather small, which is exactly why every case of effective Hamiltonian yielding an analytical result is important. Besides an academic value, it provides a way to observe similarities in electron properties between different models in various dimensions, by changing the parameters of the initial

Preprints (www.preprints.org) | NOT PEER-REVIEWED | Posted: 31 October 2023 doi:10.20944/preprints202310.2091.v1

Hamiltonian promoted into the final result, precisely addressing the underlying mechanisms leading to them.

In this paper we define and analyse the two-band effective Hamiltonian capable of describing two different electronic ground states (phases). The first one is the nodal-loop phase (NLP) and it is characterised by the touching of the valence bands over a ring. The second one is the gapped phase (GP) characterised by separation of the valence bands by a finite energy gap. We find the corresponding electron dispersions for both phases and assume that the doping procedure (Fermi energy shifting) leaves the valence bands intact. We analyse the Fermi surface (FS) for each phase together with the identification of the van Hove points. Electron dispersions are presented in terms of dimensionless variables in which their properties are determined by a single parameter λ. It is shown that the NLP has a torus-like FS which, depending on parameter λ, can be doughnut-like or self-intersecting spindle, while the FS in the case of GP has trivial shape related to usual doped 3D insulators. The DOS calculations are performed by finding the corresponding integration boundaries for each phase. Finally the expressions for DOS in both phases are given. DOS of the both phases is analysed in detail, with particular emphasis on the behaviour near van Hove points and in connection to the parameter λ, where DOS in the NLP showed a richer structure compared to the GP. It is our intention to use the two-band model in order to shed additional light upon otherwise complicated band structures that is inherent to majority of the nodal-line systems [20,21].

2. The two-band Hamiltonian

The low-energy Hamiltonian of the 3D system under consideration, in the basis of the plane waves characterized by the wave vector $\mathbf{k} = (k_x, k_y, k_z)$, presented as a real 2×2 matrix, reads

$$\hat{H} = (\Delta + \nu b k^2)\sigma_z + c k_z \sigma_x. \tag{1}$$

In the above expression, σ_z and σ_x are the Pauli matrices, while Δ, b and c are positive parameters. Index $\nu = \pm 1$ is the phase index with $\nu = -1$ denoting the NLP and $\nu = +1$ denoting the GP. Hamiltonian (1) contains square of the total Bloch wave vector $k^2 = k_x^2 + k_y^2 + k_z^2$. The diagonalization of Equation (1) is straightforward, yielding an electron-hole symmetric eigenvalues for each phase ν,

$$\varepsilon_\nu^\pm(\mathbf{k}) = \pm\sqrt{(\Delta + \nu b k^2)^2 + c^2 k_z^2}. \tag{2}$$

We scale electron dispersion Equation (2) to the gap parameter Δ, introducing dimensionless variables $\omega_\nu^\pm(\boldsymbol{\kappa}) = \varepsilon_\nu^\pm(\mathbf{k})/\Delta$, $\boldsymbol{\kappa} = \sqrt{b/\Delta}\,\mathbf{k}$ (i.e. $\kappa^2 = k^2 b/\Delta$) and parameter $\lambda^2 = c^2/(b\Delta)$. We obtain the dispersions Equation (2) in dimensionless form

$$\omega_\nu^\pm(\boldsymbol{\kappa}) = \pm\sqrt{(1 + \nu\kappa^2)^2 + \lambda^2\kappa_z^2} \tag{3}$$

determined by two parameters: (1) the phase parameter $\nu = \pm 1$ essentially controlling the band topology, and (2) parameter λ that controls physical properties of bands, such as van Hove points, effective mass parameters etc. Below we provide a detailed description of band properties.

3. Valence bands and Fermi surface

Here we investigate properties of electron dispersions Equation (3) and the Fermi surface in a doped system. Initially we assume that both phases are undoped, i.e. that the Fermi level is located between the bands. The doping procedure consists of filling the conduction band $\omega_\nu^+(\boldsymbol{\kappa})$ up to some finite value of Fermi energy ω_F (in units of Δ). Analytical analysis of the dispersion relation leads to the ν-dependent polynomial in λ,

$$P_\nu(\lambda) = \frac{\lambda^4}{4} + \nu\lambda^2, \tag{4}$$

doi:10.20944/preprints202310.2091.v1

appearing to be important for further calculations and description of the spectral properties as well as the DOS (it is shown in Figure 1). For $\nu = -1$ (NLP), $P_-(\lambda)$ is non-monotonic function, i.e. $P_-(\lambda) \lesseqgtr 0$ for $\lambda \lesseqgtr 2$, with minimum at $P_-(\lambda = \sqrt{2}) = -1$, while for $\nu = +1$ (GP), $P_+(\lambda)$ is positive monotonic function.

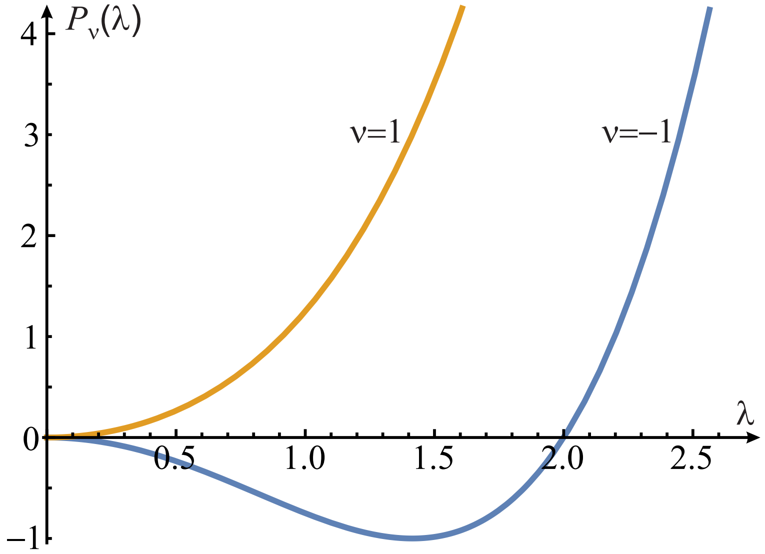

Figure 1. The $P_\nu(\lambda)$ polynomial according to Equation (4).

3.1. *The nodal-loop phase (NLP)*

This phase appears for $\nu = -1$. In the intrinsic case, when the Fermi energy $\omega_F = 0$, the main property of the NLP is presence of the nodal ring of radius $\kappa_0 = 1$ located in the (κ_x, κ_y) plane along the touching line of two bands (3). If ω_F is increased, a doughnut-like Fermi surface emerges (see Figure 2). Exact properties of this Fermi surface depend on the value of parameter λ. There are two cases to be closely examined:

a) Case $\lambda \in (0, \sqrt{2})$: The Fermi surface is shown in Figure 2a. As the Fermi energy ω_F increases from zero, the point-like (the nodal point) cross-section, along the $\kappa_x = 0$, or $\kappa_y = 0$ plane, evolves to two crescent shapes. As ω_F further increases, the crescent shapes are inflated and eventually touch each other, forming two self-intersecting circles. The FS at this particular Fermi energy ω_T is a type of torus called the self-intersecting spindle. The energy $\omega_T = \sqrt{-P_-(\lambda)}$ at which it occurs is the van Hove saddle point. The radius of each self-intersecting circles is $r = (\sqrt{1+\omega_T} + \sqrt{1-\omega_T})/2$ while their centers are displaced by $2R = \sqrt{1+\omega_T} - \sqrt{1-\omega_T}$ apart. For such a torus, it is evident that $R < r$. As ω_F increases further, the FS becomes composed of two ellipsoid-like surfaces (smaller one centered inside the bigger one) one decreasing and other increasing in size until $\omega_F = 1$ is reached. At $\omega_F = 1$, there appears an elliptic van Hove point, at which the FS is a single ellipsoid-like surface. In the special case $\lambda = 0$, the two bands touch over a sphere of radius $\kappa_0 = 1$. Then, if the Fermi energy is $0 < \omega_F < 1$, the FS comprises of two concentric spheres and, if $\omega_F > 1$, the FS is a single sphere.

b) Case $\lambda \in (\sqrt{2}, 2)$: The Fermi surface is shown in Figure 2b. As ω_F increases, the thickens of the "doughnut" reaches a special value when its cross-section with a plane $\kappa_x = 0$, or $\kappa_y = 0$ are two circles, i.e. the FS becomes a torus. As in previous case, this happens at the particular value of Fermi energy, $\omega_T = \sqrt{-P_-(\lambda)}$. In this case the FS forms a standard torus with radius of the circular cross-section $r = (\sqrt{1+\omega_T} - \sqrt{1-\omega_T})/2$ and radius from the center of the torus to the center of the cross-section $R = (\sqrt{1+\omega_T} + \sqrt{1-\omega_T})/2 > r$. As ω_F is increased with respect to ω_T, two circles of the cross-section inflate, deform and touch each other at $\omega_F = 1$. This point is

doi:10.20944/preprints202310.2091.v1

the van Hove saddle point, which is responsible for the kink in DOS of the 3D system as we shall show later. As ω_F is further increased, the FS attains an ellipsoidal-like shape.

c) Case $\lambda > 2$: The Fermi surface shows no distinctive, or interesting features other than compact doughnut-like shape. We do not show it graphically.

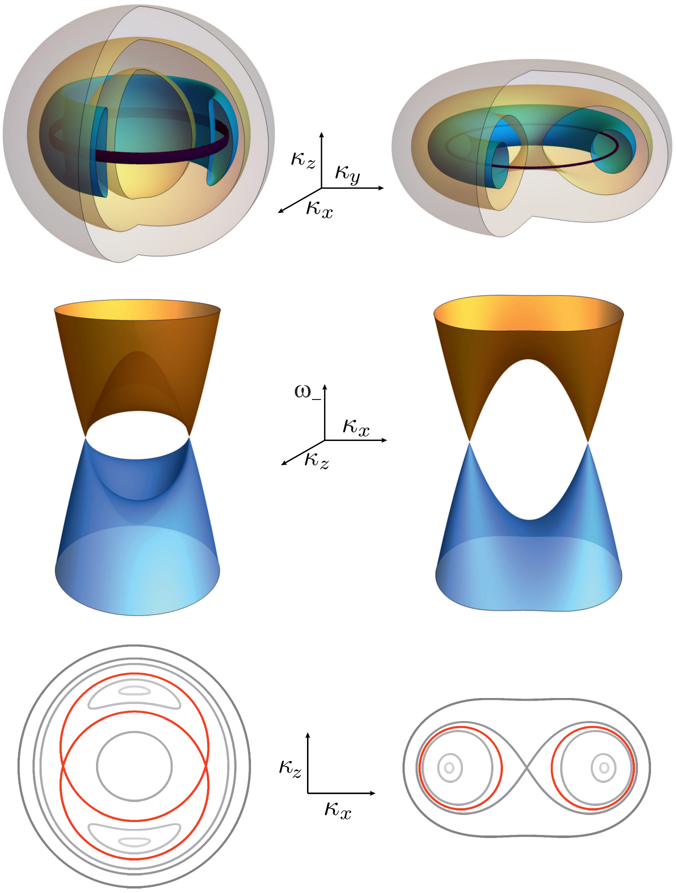

(a) **(b)**

Figure 2. The NLP phase. The 3D Fermi surface (upper panel), the band energy, $\omega_-^+(\boldsymbol{\kappa})$ (brown) and $\omega_-^-(\boldsymbol{\kappa})$ (blue), dependence at $\kappa_y = 0$ (middle panel), and its cross-section in the (κ_x, κ_z) plane (i.e. $\kappa_y = 0$) (lower panel), determined by electron dispersion Equation (3). The FSs are shown at different dopings, i.e. the different value of the Fermi energy ω_F, for: (a) $\lambda = 0.5 \in (0, \sqrt{2})$ and (b) $\lambda = 1.7 \in (\sqrt{2}, 2)$. The Fermi energies ω_F in cross-sections are (in ascending shades of gray from light to dark): 0.1, 0.3, 0.8, 1 and 1.5. The red contour is for $\omega_F = \omega_T(\lambda)$, i.e. 0.4841 in (a) and 0.8955 in (b).

3.2. The gapped phase (GP)

This phase appears for $\nu = +1$. Dominated by the band gap parameter Δ, the FS of a doped gapped phase becomes a simple ellipsoid-like structure existing only for $\omega_F > 1$ (see Figure 3a), in which parameter λ increases the axial anisotropy, i.e. the larger is λ, the flatter is the ellipsoid (see Figure 3b). In fact, it can be shown that the FS can be, to an excellent approximation, written in terms of the reduced ellipsoid equation with the coefficients depending on the Fermi energy ω_F (measured from the middle of the band gap) and parameter λ,

$$\frac{\kappa_x^2}{\omega_F - 1} + \frac{\kappa_y^2}{\omega_F - 1} + \frac{\kappa_z^2}{\sqrt{\omega_F^2 + P_+(\lambda)} - \sqrt{1 + P_+(\lambda)}} = 1. \tag{5}$$

Comparison of $\kappa_x = 0$ or $\kappa_y = 0$ plane cross section of (3) and (5) for various ω_F and λ is shown in Figure 3b. In the special case $\lambda = 0$, Equations (3) and (5) reduce to equation for sphere with radius $\kappa_0 = \sqrt{\omega_F - 1}$.

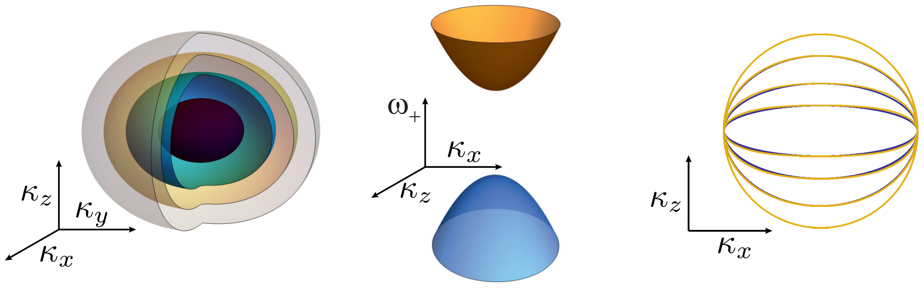

(a) **(b)**

Figure 3. The GP phase. (a) The 3D Fermi surface, for different values of $\omega_F > 1$ (left panel), and the band energy, $\omega_+^+(\boldsymbol{\kappa})$ (brown) and $\omega_+^-(\boldsymbol{\kappa})$ (blue), dependence at $\kappa_y = 0$ (right panel), determined by electron dispersion Equation (3). (b) The FS cross-section in the (κ_x, κ_z) plane at the Fermi energy $\omega_F = 3.5$ for different $\lambda = 0, 2, 4, 8$ (rounder to flatter ellipses). The yellow curve is the exact result from Equation (3) while the blue curve is an approximation Equation (5).

Electron bands (3) in both, NLP and GP phases are shown in Figure 4.

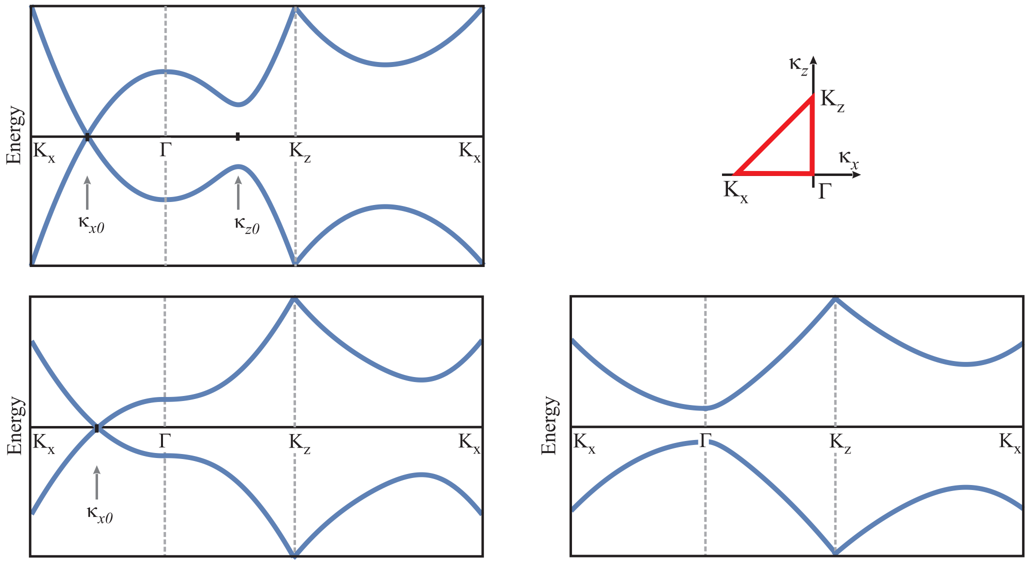

(a) **(b)**

Figure 4. Electron bands (3) in (a) NLP ($\nu = -1$) and (b) GP ($\nu = +1$) phase along the characteristic directions in the momentum space (see the inset). The $\Gamma = (0, 0)$ point is in the origin of momentum space, while K$_{x,z}$ are some points equally far away from the origin. Since the energy dependence on κ_x and κ_y are equivalent, all energies are plotted as $\omega_\nu^\pm(\kappa_x, \kappa_y = 0, \kappa_z)$. Bands ω^+ (upper) and ω^- (lower) posses the electron-hole symmetry. For the NLP case (a), the parameter values are $\lambda = 0.5 < \sqrt{2}$ (upper panel) and $\lambda = 1.7 > \sqrt{2}$ (lower panel). There are two characteristic points, the nodal point $\kappa_{x0} = 1$ and point $\kappa_{z0} = (1 - \lambda^2/2)^{1/2}$. For the GP case, the parameter value is $\lambda = 3$.

4. Density of states

Here we present calculation of the density of states (DOS) for the energy dispersion from Equation (2) for both NLP and GP. Due to the electron-hole symmetry we use only the upper band $\varepsilon_\nu^+(\mathbf{k})$ in the calculations. By definition, the DOS per unit volume of a spin degenerate band is [22]

$$N_\nu(\varepsilon) = \frac{2}{V}\sum_{\mathbf{k}} \delta(\varepsilon - \varepsilon_\nu^+(\mathbf{k})). \tag{6}$$

To simplify further calculation we use the dimensionless variables defined in Section 2 and, changing the sum in Equation (6) to an integral in spherical coordinate system, we get

$$N_\nu(\omega) = \frac{1}{2\pi^2}\sqrt{\frac{\Delta}{b^3}} \int \kappa^2\, d\kappa \int_0^\pi \sin\theta d\theta \delta\left(\omega - \sqrt{(1+\nu\kappa^2)^2 + \lambda^2\kappa^2\cos^2\theta}\right). \tag{7}$$

To further evaluate (7) we decompose the δ-function with respect to the θ variable into a sum

$$\delta\left(\omega - \sqrt{(1+\nu\kappa^2)^2 + \lambda^2\kappa^2\cos^2\theta}\right) = \sum_{\theta_0} \delta(\theta - \theta_0)\frac{\omega}{|\lambda^2\kappa^2\cos\theta_0\sin\theta_0|}, \tag{8}$$

where θ_0 are the two zero-points of the argument of the δ-function with respect to variable θ,

$$\theta_0 = \pm \mathrm{Arccos}\sqrt{\frac{\omega^2 - (1+\nu\kappa^2)^2}{\lambda^2\kappa^2}}. \tag{9}$$

Using the identities Equations (9) and (8) with Equation (7), with substitution $u = \kappa^2$, we obtain

$$N_\nu(\omega) = \frac{1}{2\pi^2}\sqrt{\frac{\Delta}{b^3}}\frac{\omega}{\lambda}\int_{\mathcal{I}} \frac{du}{\sqrt{\omega^2 - (1+\nu u)^2}}. \tag{10}$$

The interval of u-integration $\mathcal{I}$ is determined by three restrictions which are enumerated here:

① $u \geq 0$ (the trivial restriction),
② positive expression under the square root in denominator in (10): $\omega^2 - (1+\nu u)^2 \geq 0$,
③ domain restriction in (9): $0 \leq \cos^2\theta_0 \leq 1$ implying $0 \leq \omega^2 - (1+\nu u)^2 \leq \lambda^2 u$.

By common intersection of these three conditions, the intervals of integration are found, which depend on phase ν, on energy ω and parameter λ. From here on we investigate the DOS for every electronic phase separately.

5. Density of states in the nodal-loop phase

We set $\nu = -1$ in the mentioned restrictions to find the permitted value of u. Thus we get:

① $u \in [0, \infty\rangle$,
② $u \in [1-\omega, 1+\omega]$,
③ $u \in \langle -\infty, 1 - \psi_+^-(\omega,\lambda)] \cup [1 - \psi_-^-(\omega,\lambda), \infty\rangle$.

In the above conditions we have introduced an auxiliary function $\psi_\pm^\nu(\omega,\lambda)$ defined as

$$\psi_\pm^\nu(\omega,\lambda) = \frac{\lambda^2}{2} \pm \sqrt{\omega^2 + P_\nu(\lambda)} \tag{11}$$

where, again, $P_\nu(\lambda)$ is given by (4). The final condition for the interval of u-integration is found by taking the intersection $u \in$ ①∩②∩③. The boundaries in ② and ③ depend on ω and λ and, for specific values of those two parameters, they will shift relatively to each other giving the different intersection. It is shown, after rather tedious calculation, that, depending on value of parameter λ, the interval of allowed values of u falls in two classes:

$$\begin{array}{ll}
\text{1.)}\ \ \lambda < \sqrt{2} & \\
0 < \omega < \omega_T, & u \in [1-\omega, 1+\omega] \\
\omega_T < \omega < 1, & u \in [1-\omega, 1-\psi_+^-(\omega,\lambda)] \cup [1-\psi_-^-(\omega,\lambda), 1+\omega] \\
\omega > 1, & u \in [1-\psi_-^-(\omega,\lambda), 1+\omega] \\
 & \\
\text{2.)}\ \ \lambda > \sqrt{2} & \\
0 < \omega < 1, & u \in [1-\omega, 1+\omega] \\
\omega > 1, & u \in [1-\psi_-^-(\omega,\lambda), 1+\omega]
\end{array} \tag{12}$$

where we have used $\omega_T = \sqrt{-P_-(\lambda)}$ from Section 3. The integration boundaries in integral (10) are determined by expressions (12), while the primitive function is of the form

$$\int \frac{du}{\sqrt{\omega^2-(1-u)^2}} = -\mathrm{Arctan}\frac{1-u}{\sqrt{\omega^2-(1-u)^2}} \tag{13}$$

Applying the above, frequently using the identity

$$\frac{\pi}{2} - \mathrm{Arctan}\frac{a}{\sqrt{\omega^2-a^2}} = \mathrm{Arccos}\frac{a}{\omega}, \tag{14}$$

we finally obtain the result

$$\begin{aligned}
N_-(\omega,\lambda) = N_0\frac{\omega}{\lambda}\Bigg[&1-\frac{1}{\pi}\mathrm{Arccos}\frac{\psi_-^-(\omega,\lambda)}{\omega}\,\Theta(\omega-1) \\
&+\frac{1}{\pi}\left(\mathrm{Arccos}\frac{\psi_+^-(\omega,\lambda)}{\omega}-\mathrm{Arccos}\frac{\psi_-^-(\omega,\lambda)}{\omega}\right)\Theta\left(\omega-\omega_T\right)\Theta(1-\omega)\Theta\left(\sqrt{2}-\lambda\right)\Bigg],
\end{aligned} \tag{15}$$

where the constant factor is

$$N_0 = \frac{1}{2\pi}\sqrt{\frac{\Delta}{b^3}}. \tag{16}$$

The constraints on ω and λ in (12) appear in terms of the Heaviside Θ-functions in Equation (15). Also notice that, for $\lambda > \sqrt{2}$, the third contribution vanishes. The DOS (15) is shown in Figure 5 as a function of ω for several values of parameter λ.

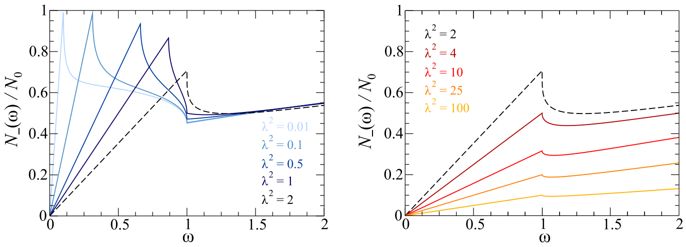

(a) **(b)**

Figure 5. Density of states of the nodal semimetal ($\nu = -1$) with energy dispersion Equation (3)) as a function of scaled energy (ω). (a) DOS in the case of self-intersecting spindle phase, appearing for $\lambda < \sqrt{2}$, shown for several values λ. (b) DOS in the torus phase of the nodal system, appearing for $\lambda > \sqrt{2}$, shown for several values λ. Black dashed curve in each graph depicts the separatrix, $\lambda = \sqrt{2}$, between regimes (a) and (b).

Also, in the vicinity of high symmetry points, we expand Equation (15) using the approximative Taylor expansion for $x \ll 1$,

$$\mathrm{Arccos}\left[\pm(1-x)\right] \approx (1\mp 1)\frac{\pi}{2} \pm \sqrt{2x}. \tag{17}$$

First, we analyse the intersecting spindle case, for $\lambda < \sqrt{2}$ (Figure 5a). The $N_-(\omega, \lambda < \sqrt{2}) = N_0\omega/\lambda$ function is linear in ω from $\omega = 0$ up to $\omega = \omega_T$ where the van Hove singularity, due to presence of the saddle point in spectrum, is located. The DOS at this point is $N_-(\omega_T, \lambda) = N_0\omega_T/\lambda$ while, for ω just above ω_T, Equation (15) can be expanded to

$$N_-(\omega \gtrapprox \omega_T, \lambda < \sqrt{2}) \approx N_0\sqrt{1-\frac{\lambda^2}{4}}\left[1-\frac{1}{\pi}\sqrt{\frac{8}{\lambda}}\left(\frac{1+\lambda^2/2}{1-\lambda^2/2}\right)^{1/4}\sqrt{\omega-\omega_T}\right]. \tag{18}$$

For $\omega > \omega_T$, DOS monotonically decreases until the next van Hove singularity, due to presence of the elliptic point in spectrum at $\omega = 1$, is reached. Since $\omega = 1$ is a limiting point that divides two-surfaced and a single-surfaced FS, we inspect in detail the corresponding DOS. Inserting $\omega = 1$ in Equation (15) we obtain

$$N_-(\omega = 1, \lambda) = \frac{N_0}{\lambda}\left[1-\frac{1}{\pi}\mathrm{Arccos}\left(\frac{\lambda^2}{2}-\left|1-\frac{\lambda^2}{2}\right|\right)\right]. \tag{19}$$

Equation (19) is shown in Figure 6 (inset). For $\lambda < \sqrt{2}$ it increases as function of λ forming a cusp for $\lambda = \sqrt{2}$, after which it decreases as $N_-(\omega = 1, \lambda > \sqrt{2}) = N_0/\lambda$.

In the high-energy limit, $\omega \gg 1$, only the first two terms in Equation (15) remain. Expanding $\psi_-^-(\omega \gg \lambda, \lambda)/\omega \approx \lambda^2(\omega - P_-(\lambda)/\lambda^2)/(2\omega^2) - 1$, and using the expansion (17), we obtain

$$N_-(\omega \gg 1, \lambda < \sqrt{2}) \approx \frac{N_0}{\pi}\sqrt{\omega - \frac{P_-(\lambda)}{\lambda^2}} \sim \sqrt{\omega}. \tag{20}$$

Equation (20) is similar to DOS of the 3D free electron gas. This result is to be expected since, for large wave vectors (i.e. the large energy), the dispersion (3) becomes roughly parabolic in wave vector since the κ^4 term dominates over the κ_z^2 term.

Some results, found for DOS in the case of intersecting torus, apply for the "doughnut torus" case, $\lambda > \sqrt{2}$. The third term in the Equation (15) vanishes, and what remains is DOS linear in ω, i.e. $N_-(\omega, \lambda > \sqrt{2}) = N_0\omega/\lambda$, for $\omega < 1$. For $\omega = 1$, DOS has a discontinuity as shown by Equation (19), and, just above $\omega = 1$, it has a square root dependence,

$$N_-(\omega \gtrapprox 1, \lambda > \sqrt{2}) \approx \frac{N_0}{\lambda}\left[1-\frac{1}{\pi}\sqrt{\frac{2\lambda^2}{\lambda^2-2}}\sqrt{\omega-1}\right], \tag{21}$$

which diverges for $\lambda = \sqrt{2}$ and therefore signals that additional elements have to be retained in the expansion of $\psi_-^-(\omega, \lambda)$. Thus, for $\lambda = \sqrt{2}$, the result up to the leading order in ω is

$$N_-(\omega \gtrapprox 1, \lambda = \sqrt{2}) \approx \frac{N_0}{\sqrt{2}}\left[1-\frac{2^{3/4}}{\pi}(\omega-1)^{1/4}\right], \tag{22}$$

where it is worth noticing the analytical property that DOS depends on the forth root of energy, appearing only in this case. Finally, in the high-energy limit, $N_-(\omega \gg 1, \lambda > \sqrt{2})$ follows the square root dependence given by Equation (20).

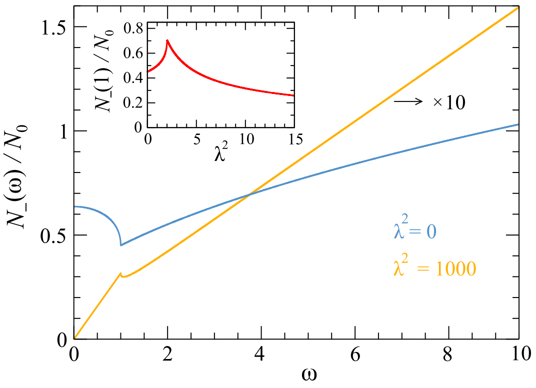

Figure 6. DOS in the NLP phase for two special cases: (1) $\lambda \gg 1$ & $\lambda \gg \omega$, according to Equation (23); (2) $\lambda = 0$, according to Equation (26). The inset shows DOS taken at the "critical point" $\omega = 1$, depending on parameter λ^2, according to Equation (19).

We also single out two specific cases:

1. The first one is for energy ω that satisfies inequality $\lambda \gg 1$ & $\lambda \gg \omega$. It is shown in Figure 6, the $\lambda^2 = 1000$ case. In this interval, the auxiliary function $\psi_-^-(\lambda \gg \omega) \to 0$, so the Equation (15) reduces to

$$N_-(\lambda \gg \omega, \lambda \gg 1) \approx N_0 \frac{\omega}{\lambda} \times \begin{cases} 1, & \omega < 1 \\ 1/2, & \omega > 1. \end{cases} \tag{23}$$

DOS in this case is linear in ω, with different slopes below and above $\omega = 1$, and highly reduced in amplitude. This property of linearity, especially in the $\omega > 1$ case, is particularly noticeable for small parameter Δ in Equation (2) if other bands are much higher (lower) in energy compared to Δ. In this limit, this 3D system effectively resembles to the 2D behaviour (see results for DOS in Ref. [24]).

2. The second specific case is for $\lambda = 0$. It is a case when Hamiltonian (1) is given only by the first term featuring the σ_z Pauli matrix. Diagonalisation leads to energies [15]

$$\omega_\kappa^\pm = \pm \left|1 - \kappa^2\right|. \tag{24}$$

Although trivial in appearance, dispersion (24) leads to the unique properties of the corresponding DOS. To see them, we analyse Equation (15) in which the third term can be written as

$$\operatorname{Arccos} \frac{\psi_+^-(\omega,\lambda)}{\omega} - \operatorname{Arccos} \frac{\psi_-^-(\omega,\lambda)}{\omega} = \operatorname{Arccos}\left(\frac{\lambda^2}{\omega^2}\left(1 + \sqrt{1-\omega^2}\right) - 1\right). \tag{25}$$

Setting the $\lambda \to 0$ in the above expression and using expansion (17) together with equation (20) in which $\lim_{\lambda \to 0} P_-(\lambda)/\lambda^2 = -1$ we obtain [15]

$$N_-(\omega, \lambda = 0) = \frac{N_0}{\pi}\left[\left(\sqrt{1+\omega} + \sqrt{1-\omega}\right)\Theta(1-\omega) + \sqrt{1+\omega}\,\Theta(\omega - 1)\right]. \tag{26}$$

This special form of DOS is shown in Figure 6 with the dome-like feature for ω below 1. This can be seen as a natural limit of the trend shown in Figure 5 as λ is decreasing.

6. Density of states in the gapped phase

Here we investigate DOS of the gapped phase by setting $\nu = +1$ in the restrictions enumerated in Section 4, obtaining permitted intervals of u-integration for each case:

① $u \in [0, \infty\rangle$,
② $u \in [-1-\omega, -1+\omega]$,

③ $u \in \langle -\infty, 1 - \psi_+^+(\omega,\lambda)] \cup [1 - \psi_-^+(\omega,\lambda), \infty\rangle$.

In the conditions above, an auxiliary function (11) is implemented and the intersection $u \in$ ①∩②∩③ determines the integration boundaries. We remind that in the GP, $\omega > 1$ (i.e. the band is located above the band gap), which makes the integration boundaries easy to determine:

$$u \in [1 - \psi_-^+(\omega,\lambda), \, -1 + \omega]. \tag{27}$$

Inserting the integration boundaries (27) in (10), and using (13) and (14), we obtain DOS in the GP phase,

$$N_+(\omega,\lambda) = N_0 \frac{\omega}{\lambda}\left[1 - \frac{1}{\pi}\mathrm{Arccos}\frac{\psi_-^+(\omega,\lambda)}{\omega}\right]\Theta(\omega - 1), \tag{28}$$

shown in Fig 7. As in the NLP case, we can determine the limiting values.

First, by expanding the expression (28) for energies just above the band gap, i.e. $\omega \gtrapprox 1$, we obtain

$$N_+(\omega \gtrapprox 1,\lambda) \approx \frac{N_0}{\pi\sqrt{1+\lambda^2/2}}\sqrt{\omega - 1}\,\Theta(\omega - 1). \tag{29}$$

Second, in the high energy limit, $\omega \gg \lambda \approx 1$, similarly to Equation (20), we obtain

$$N_+(\omega \gg 1,\lambda) \approx \frac{N_0}{\pi}\sqrt{\omega - \frac{P_+(\lambda)}{\lambda^2}} \sim \sqrt{\omega}. \tag{30}$$

The "square root behaviour" in both cases, resembling the 3D free electron gas, is not surprising since we work with the band with the elliptic point at its bottom.

Third, in the case of energies over which the parameter λ is the dominant variable, i.e. $\lambda > \omega$, by setting $\psi_-^+(\omega,\lambda) \to 0$ we obtain

$$N_+(\omega > 1, \lambda \gg \omega) \approx N_0\frac{\omega}{2\lambda}. \tag{31}$$

As expected, this is the same result as in Equation (23) (see Figure 7, case $\lambda = 10$), which follows from the correct expansion of Equation (3) with dominant λ-term.

Finally, let us examine the $\lambda \to 0$ limit, in which the expression (29) reduces to

$$N_+(\omega,\lambda = 0) = \frac{N_0}{\pi}\sqrt{\omega - 1}\,\Theta(\omega - 1), \tag{32}$$

which is a DOS of the 3D parabolic insulator.

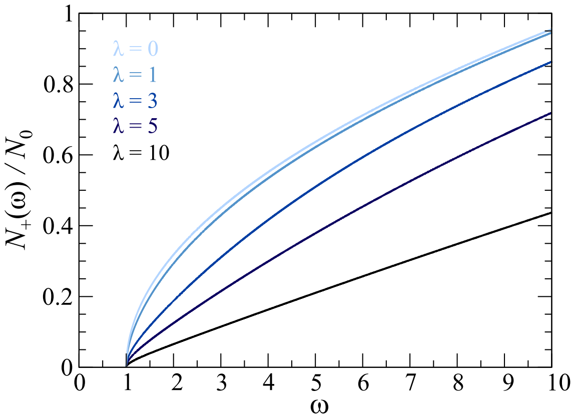

Figure 7. Density of states in the gapped phase ($\nu = +1$) of the system, with energy dispersion Equation (3) as a function of scaled energy ω, for different values of parameter λ, according to Equation (28).

7. Conclusion

We present analytical results comprising electron bands and density of states (DOS) for the effective low-energy two-band electron Hamiltonian, which models the so-called nodal-loop phase (NLP) and the gapped phase (GP) depending on parameters. This way to model the real materials is quite common and useful for description of response to the low-energy excitations, the most common among them the different types of transport properties, such as optical conductivity for example, for systems with two bands close to the Fermi energy. Beside the common models, where the density of state naturally appears, such as the plasmon properties, Coulomb screening or superconductivity mechanisms, it has recently been shown that it plays a key role in description of the dynamical charge transport in the Holstein-like systems in which it turns out that electron relaxation can be described solely in terms of electron DOS [25]. In that sense, an analytical character of DOS, presented in this paper for the considered Hamiltonian, is of an utmost importance in order to understand the underlying mechanisms leading to properties of the above-mentioned quantities depending on it.

In this paper we present analysis of exactly those features. We observe a vanishing value of DOS at the Fermi energy (in the intrinsic case), followed by the linear increase with energy in the NLP case, typical for semimetalic systems, or square-root behaviour above the bottom of the band in the GP case, characteristic for 3D insulators with parabolic electron dispersion. Also, we provide a detailed description of DOS around the van Hove singularities appearing due to presence of the peculiar points in electron spectrum. In the NLP case the hyperbolic (saddle) point and the elliptic point are encountered, while the GP case features only the elliptical point at the bottom of the band. The good analysis of similar Hamiltonian with the NLP, from its topological properties to the real materials described by it, is given in Refs. [1,26]. On the other hand, an example of application of the NLP Hamiltonian to description of the optical conductivity is given in Refs. [23,27]. The band structure of the corresponding real systems can be quite complex, usually addressed by different *ab initio* methods [20,21]. This work is to complement those methods by the precise, analytical description of the bands and DOS properties in the most relevant region - the narrow interval around the Fermi energy located either in the vicinity of the nodal line or the band gap.

Author Contributions: Z.R., I.K. and D.R. contributed to this paper in terms of conceptualization, methodology, formal analysis and draft preparation. All authors have read and agreed to the published version of the manuscript.

Funding: This research was funded by the QuantiXLie Centre of Excellence, a project co-financed by the Croatian Government and European Union through the European Regional Development Fund — the Competitiveness and Cohesion Operational Programme (Grant KK.01.1.1.01.0004), and by the Scientific Exchange grant IZSEZ0_217543.

Conflicts of Interest: The authors declare no conflict of interest whatsoever.

References

1. Yang, S. -Y., Yang, H., Derunova, E., Parkin, S. S. P., Yan, B. and Ali, M. N. Symmetry demanded topological nodal-line materials. *Advances in Physics: X* VOL. 3, NO.1, 1414631 (2018)
2. Bernevig, B. A., Hughes, T.L., Zhang, S.C. Quantum Spin Hall Effect and Topological Phase Transition in HgTe Quantum Wells. *Science* **314**, 1757–1761 (2006).
3. Su, W.P., Schrieffer, J.R. and Heeger, A.J. Solitons in Polyacetylene. *Phys. Rev. Lett.* **42**, 1698-1701 (1979).
4. Peierls, R.E. *Quantum Theory of Solids*, Clarendon Press, Oxford (1955), pp. 108.
5. Jafari, S. A. Nonlinear optical response in gapped graphene. *J. Phys.: Condens. Matter* **24**, 205802 (2012).
6. Wallace, P.R. The Band Theory of Graphite. *Phys. Rev.* **71**, 622 (1947).
7. Kupčić, I. Damping effects in doped graphene: The relaxation-time approximation. *Phys. Rev. B* **90**, 205426-1-15 (2014).
8. Carbote, J. P. Dirac cone tilt on interband optical background of type-I and type-II Weyl semimetals. *Phys. Rev. B* **94**, 165111 (2016).
9. Montambaux, G., Piechon, F., Fuchs, J. N., Goerbig, M. O. Merging of Dirac points in a two-dimensional crystal. *Phys. Rev. B* **80**, 153412 (2009).

10. Mukherjee, D. K., Carpentier, D., Goerbig, M. O. Dynamical conductivity of the Fermi arc and the Volkov-Pankratov states on the surface of Weyl semimetals. *Phys. Rev. B* **100**, 195412 (2019).
11. Rukelj, Z., Homes, C.C., Orlita, M., Akrap, A. Distinguishing the gapped and Weyl semimetal scenario in $ZrTe_5$: Insights from an effective two-band model. *Phys. Rev. B* **102**, 125201 (2020).
12. Polatkan, S., Goerbig, M. O., Wyzula, J., Kemmler, R., Maulana, L.Z., Piot, B. A., Crassee, I., Akrap, A., Shekhar, C., Felser, C., Dressel, M., Pronin, A. V., Orlita, M. Magneto-Optics of a Weyl Semimetal beyond the Conical Band Approximation: Case Study of TaP. *Phys. Rev. Lett.* **124**, 176402 (2020).
13. Ashby, P.E.C., Carbotte, J.P. Chiral anomaly and optical absorption in Weyl semimetals. *Phys. Rev. B* **89**, 245121 (2014).
14. Peres, N.M., Santos, J.E. Strong light–matter interaction in systems described by a modified Dirac equation. *J. Phys.: Condens. Matter* **25**, 305801 (2013).
15. Rukelj, Z., Akrap, A. Carrier concentrations and optical conductivity of a band-inverted semimetal in two and three dimensions. *Phys. Rev. B* **104**, 075108-1-12 (2021).
16. Rukelj, Z., Radić, D. Topological Properties of the 2D 2-Band System with Generalized W-Shaped Band Inversion. *Quantum Rep.* **4**, 476–485 (2022).
17. Barati, S., Abedinpour, S.H. Optical conductivity of three and two dimensional topological nodal-line semimetals. *Phys. Rev. B* **96**, 155150 (2017).
18. Rukelj, Z., Radić, D. DC and optical signatures of the reconstructed Fermi surface for electrons with parabolic band. *New J. Phys.* **24**, 053024-1-16 (2022).
19. Dressel, M., Grüner, G. *Electrodynamics of Solids: Optical Properties of Electrons in Matter*, Cambridge University Press, 2002.
20. Bian, G., Chang, T. R., Zheng, H., Velury, S., Xu, S. Y., Neupert, T., Chiu, C. K., Huang, S. M., Sanchez, D. S., Belopolski, I., Alidoust, N., Chen, P. J., Chang, G., Bansil, A., Jeng, H. T., Lin, H. and Hasan M. Z. Drumhead surface states and topological nodal-line fermions in $TlTaSe_2$. *Phys. Rev. B* **93**, 121113(R) (2016).
21. Wang, X., Ding, G., Cheng, Z., Surucu, G., Wang, X. L., Yang, T. Novel topological nodal lines and exotic drum-head-like surface states in synthesized CsCl-type binary alloy TiOs. *Journal of Advanced Research* **22**, 137-144 (2020).
22. Ashcroft, N. W. and Mermin, N. *Solid State Physics*, Saunders Collage, 1976.
23. Yang, M. X., Luo, W. and Chen, W. Quantum transport in topological nodal-line semimetals. *Advances in Physics: X* VOL. 7, NO.1, 2065216 (2022).
24. Carbote, J. P., Nicol, E. J. Signatures of merging Dirac points in optics and transport. *Phys. Rev. B* **100**, 035441 (2019).
25. Rukelj, Z. *et al.* to be published (accepted in the *Phys. Rev. B*).
26. Fang, C., Weng, H., Dai, X. and Fang Z. Topological nodal line semimetals, *Chinese Phys. B* **25**, 117106 (2016).
27. Kandel, S., Gumbs, G. and Berman, O.L. Optical Response of 3D Model Topological Nodal-line Semimetal. *Advances in Nanosheets*. IntechOpen, Jun. 28, 2023. doi: 10.5772/intechopen.1001440.